Electric generation and ratcheted transport of contact-charged drops

Charles A. Cartier, Jason R. Graybill, and Kyle J. M. Bishop

Electric Generation and Ratcheted Transport of Contact-Charged Drops

Charles A. Cartier and Jason R. Graybill

Department of Chemical Engineering, The Pennsylvania State University, University Park, PA 16802, USA

Kyle J. M. Bishop*

Department of Chemical Engineering, Columbia University, New York, NY 10027, USA

(Dated: September 18, 2017)

We describe a simple microfluidic system that enables the steady generation and efficient transport of aqueous drops using only a constant voltage input. Drop generation is achieved through an electrohydrodynamic dripping mechanism by which conductive drops grow and detach from a grounded nozzle in response to an electric field. The now-charged drops are transported down a ratcheted channel by contact charge electrophoresis (CCEP) powered by the same voltage input used for drop generation. We investigate how the drop size, generation frequency, and transport velocity depend on system parameters such as the liquid viscosity, interfacial tension, applied voltage, and channel dimensions. The observed trends are well explained by a series of scaling analyses that provide insight into the dominant physical mechanisms underlying drop generation and ratcheted transport. We identify the conditions necessary for achieving reliable operation and discuss the various modes of failure that can arise when these conditions are violated. Our results demonstrate that simple electric inputs can power increasingly complex droplet operations with potential opportunities for inexpensive and portable microfluidic systems.

PACS numbers: 47.55.db, 47.65.-d,82.45.-h, 47.61.-k

I. INTRODUCTION

The generation and transport of droplets within microfluidic systems is essential to applications ranging from chemical and materials synthesis [1, 2] to high-throughput biological assays [3, 4]. Owing to their small size, such systems can offer advantages in cost, safety, and control by reducing reagent volumes and increasing the rates of heat and mass transfer. Moreover, confinement of species within drop-based "reactors" can enhance mixing within the drop while limiting dispersion along the length of the channel [5]. High-throughput processing of many independent droplets offers an attractive route towards screening multiple input conditions (e.g., chemical reactions [6]), quantifying stochastic processes (e.g., ice nucleation [7, 8]), and investigating heterogeneous populations (e.g., single cell assays [9]).

Most commonly, drops are created and transported by pressure-driven flows using appropriate channel geometries such as cross flow, co-flow, or flow focusing configurations [10]. These approaches allow for the steady generation of monodisperse drops at frequencies as high as 30 kHz [11]; however, they often rely on external pumps which can limit portability. Alternatively, aqueous drops can be generated on-demand and actuated in a programmable fashion using electric fields to direct drop motion via electrowetting and/or dielectrophoresis [12]. So-called digital microfluidics is particularly attractive for use in "point-of-care" diagnostic platforms that rely on small batteries to power the active components of portable systems [13]. However, the complexity and cost

of these platforms may limit their use as compared to simpler alternatives (e.g., paper-based systems [14, 15]).

Here, we describe a microfluidic system for the electric generation and ratcheted transport of aqueous drops that combines the simplicity of pressure-driven systems with the portability and versatility of electrically actuated systems. Charged droplets are generated repeatedly by application of a static electric field, which induces drop pinch-off from a dielectric nozzle upon reaching a critical size. This type of electrically powered dripping is fundamentally distinct from electrospraying [16, 17] and results in larger drops with smaller size polydispersity. A similar strategy for electric drop generation was described by Link and co-workers [18]; however, their system and its variations [19] rely on pressure-driven flows to transport drops downstream. By contrast, we show that conductive droplets can be transported away by ratcheted electrophoresis [20, 21] using the same voltage input that drives drop generation.

In this approach, the drop is repeatedly charged on contact with the surface of a biased electrode and then actuated by the electric field emanating from that electrode. This process – termed contact charge electrophoresis (CCEP) by us [20, 22, 23] or electrophoresis of a charged drop (ECD) by others [24–26] – results in the continuous oscillatory motion of the drop between two electrodes subject to a constant voltage. Importantly, this motion can be rectified by a series of dielectric ramps to achieve steady directed motions through microfluidic channels. Such ratcheted transport was previously demonstrated using conductive solid particles [20]; herein, we extend this approach to enable transport of deformable drops. Through a series of scaling analyses, we discuss the relevant physics governing the size

and frequency of electrically generated drops as well as their velocity down the ratcheted channel. We identify the conditions necessary for achieving drop generation and transport and discuss the various modes of failure that can arise when these conditions are violated. Together, our results demonstrate that simple electric inputs can power increasingly complex droplet operations with potential opportunities for creating inexpensive and portable microfluidic systems.

II. EXPERIMENTAL

The microfluidic device for electric generation and ratcheted transport of aqueous drops was fabricated in polydimethylsiloxane (PDMS) by soft lithography (Fig. 1) [27]. The device had three main components: a central ratcheted channel filled with a dielectric liquid, two gallium electrodes on either side, and a water channel that supplied an aqueous electrolyte. The central channel (width $W = 400$ μm, height $H = 100$ μm) was flanked by a periodic array of PDMS ramps designed to direct the motion of conductive drops by CCEP (side $w = \ell = 180$ μm, period $L = 215$ μm). The geometry of the ratcheted channel was similar to that used previously for transport of solid particles [20]; the specific dimensions of each device used in experiment are summarized in Table I. The electrode channels were designed to contact the liquid within the center channel thereby enabling the charging of conductive drops at the electrode surface. The water channel connected to the central channel through a narrow nozzle (width $\delta = 10$ μm). In some experiments (numbered 4 and 5 in Table I), a longer water channel was used with an estimated hydrodynamic resistance of $R_w = (3 \times 10^{17}$ m$^{-1})\eta_w$ to slow the rate of drop generation (Appendix A). The microfabricated channels were bonded to a PDMS-coated glass slide by exposure to O$_2$: He plasma for 30 s prior to sealing. The device was heated overnight at 180°C on a hotplate to restore the hydrophobicity of the channels. After heat treatment, the water contact angle on the PDMS surface was measured; only devices with contact angles greater than 90° were used. The electrodes were prepared by flowing liquid gallium at 60°C into the designated channels, cooling to room temperature, and inducing crystallization by contact with a piece of solid gallium [20, 28].

Directly prior to use, the device was positioned on the stage of an optical microscope, and the central channel primed with either mineral oil (Sigma-Aldrich M8410) or silicone oil (Sigma-Aldrich 378356). The flow of oil and water were controlled independently by pressure pumps (McMaster-Carr 1888K1 and 3834K11). After filling the channel, flow was stopped by adjusting the upstream oil pressure p_o to balance the gravitational pressure drop between the pump and microscope stage (i.e., $p_o = \rho_o g h$ where g is the acceleration due to gravity, and $h = 27$ cm was the height of the microscope stage above the pump). We further confirmed that there was no flow of oil in the
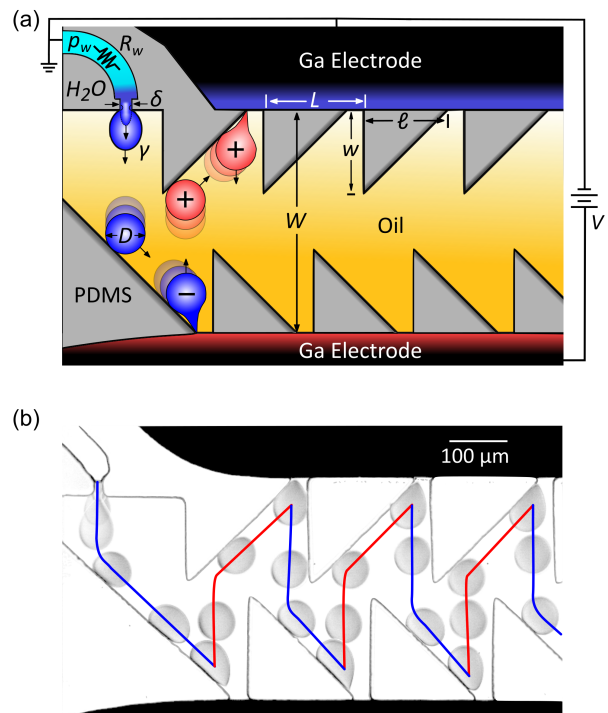

FIG. 1. (a) Schematic illustration of a microfluidic device for the electric generation and ratcheted transport of aqueous drops. The relevant dimensions of each device are listed in Table I; an additional gallium electrode (not shown) was used to ground the water channel upstream (Fig. S1) [29]. Application of a positive voltage V induces the formation of negatively charged water drops (blue) at the nozzle, which move toward the lower electrode under the influence of the field. Upon contact with the lower electrode, the drop acquires a net positive charge (red) and moves back toward the opposite electrode. The PDMS ramps rectify this oscillatory motion to transport the drop down the channel. Note that gravity is directed into the page. (b) Overlaid experimental images (Experiment 6, $V = 400$ V, $p'_w = 0.12$ psi) showing the generation and transport of a **single** water drop at consecutive time points. The solid curve shows the trajectory of the drop down the channel (see Supplemental Video 1) [29].

central channel by observing the motion (or lack thereof) of water drops therein. Silicone oil caused some swelling of the PDMS features [31]; however, these effects were accounted for when designing the channel dimensions.

The water channel was filled with an aqueous electrolyte (100 mM NaCl in deionized water) containing different concentrations $(0-2$ wt%$)$ of a non-ionic surfactant (Tween 20). For these surfactant concentrations, the measured tension of the water-oil interface ranged from $\gamma = 6 - 51$ mN/m (Fig. S2) [29]. We chose Tween 20 for its low solubility in oil, since inverse micelles in the oil phase can greatly increase the electric conductivity therein [32]. Motion via CCEP requires that the carrier fluid be sufficiently insulating as to prevent leakage of charge from the drop as it traverses the channel [30]. The presence of surfactant also helped to mitigate wet-

TABLE I. Experimental conditions for the six devices used to generate the data presented here. Experiments 1-5 were designed to investigate the role of different parameters; experiment 6 was designed to demonstrate drop generation and transport at near-optimal conditions. The physical properties of mineral oil (MO) were measured previously [30]: density, $\rho_o = 840$ kg/m^3; viscosity, $\eta_o = 0.027$ Pa s; permittivity, $\varepsilon = 2.5\varepsilon_0$; conductivity, $K \sim 10^{-12}$ S/m. Those of silicone oil (SO) were provided by the supplier: $\rho_o = 960$ kg/m^3, $\eta_o = 0.048$ Pa s, $\varepsilon = 2.7\varepsilon_0$, $K \sim 10^{-12}$ S/m).

Exp.	W (μm)	H (μm)	δ (μm)	$w = \ell$ (μm)	L (μm)	oil	η_w (mPa s)	γ (mN/m)
1	201	50	19	65	90	MO	1	51
2	197	50	15	89	115	MO	1	7
3	389	87	29	180	210	MO	1	7
4	387	95	6	179	213	SO	1	6
5	382	95	8	184	216	SO	2	6
6	388	95	12	178	214	SO	2	6

ting of the PDMS channels by the aqueous phase. The purpose of the added salt was to increase the conductivity of the aqueous solution and thereby the rate of charge transfer to/from drops on contact with the electrodes or one another. As discussed below, rapid charge transfer reduced the likelihood of drop coalescence when multiple drops were moving within the ratcheted channel [33, 34]. The inlet water pressure p_w was chosen as to position the oil-water interface at the nozzle with the applied pressure balanced by the gravitational pressure and the capillary pressure (see further discussion below). In practice, the range of pressures that could hold the interface at the nozzle was determined by slowly decreasing or increasing p_w in increments of 0.01 psi until the water receded from the water channel or flooded the central channel, respectively. Unless otherwise noted, experiments on drop generation were conducted at water pressures p_w just below the flooding pressure. We report the applied pressure less the gravitational pressure drop, $p'_w = p_w - \rho_w gh$, as this quantity determines the flow rate through the water channel.

Starting from this static configuration, a constant potential $V = 0$–1000 V was applied to the lower electrode relative to that of the upper electrode and the electrolyte, which were grounded. To mitigate potential damage due to a short circuit, the current was limited to 1 μA by a sourcemeter unit (Keithley 2410). The resulting dynamics was captured by high speed video microscopy (Phantom v310) as illustrated in the time series of overlaid images in Figure 1b. Under appropriate operating conditions, the electric stress at the oil-water interface caused the water to flow into the central channel forming a drop of water attached to the nozzle. When the drop grew to a critical size, it detached from the nozzle and moved in the electric field towards the opposite electrode. Upon contacting the electrode, the net charge on the drop changed sign, causing it to move back towards the upper electrode. Importantly, the PDMS ramps served to rectify the oscillatory motion of the drop thereby transporting it away from the nozzle and down the length of the channel. During application of the voltage, multiple drops were created and transported down the channel. The characteristics and dynamics of each drop was analyzed

to determine the drop size, shape, velocity, and frequency as a function of time. After each experiment, the central channel was flushed with oil to remove any remaining water drops, and the above procedure was repeated.

III. RESULTS & DISCUSSION

A. Drop Generation

Under appropriate conditions, drops were generated repeatedly for a period of ∼10 seconds before stopping (Fig. 2a). During this period, the drop diameter D increased as did the time interval between successive drops. We attribute this behavior to the transient screening of the applied field by mobile charge carriers in the oil phase that accumulate at the oil-PDMS interface. Consistent with this hypothesis, the duration of drop generation was similar to the charge relaxation time over which screening occurs. In both mineral and silicone oil, this time is approximately $\varepsilon/K \sim 10$ s, where ε and K are the fluid permittivity and conductivity, respectively [30].

Additionally, we note that the Debye screening length in the oil is estimated to be $\kappa^{-1} \sim 20$ μm based on the definition $\kappa = (2e^2 n/\varepsilon k_B T)^{1/2}$ where $n \sim 4 \times 10^{15}$ ions/m^3 is the ion density, estimated from the measured electrical conductivity of mineral oil as $K = e^2 n/\lambda \sim 10^{-12}$ S/m where $\lambda \sim 6\pi\eta a_i$ is an approximate ion drag coefficient (ion radius, $a_i = 0.2$ nm). This length is smaller than the electrode separation ($W = 400$ μm), indicating that screening of the field will occur. Because the applied potential is orders of magnitude larger than the thermal potential $k_B T/e$, screening by mobile charge carriers should occur primarily within a thin layer near the oil-PDMS interface rather than the diffuse double layer of thickness κ^{-1}.

We further confirmed that drop generation could be re-initiated by reversing the polarity of the applied voltage (see Supplemental Video 2) [29]. Below, we limit our discussion to experiments using a single step increase in the applied voltage. Reported measurements of the drop diameter and frequency represent averages over all drops generated.
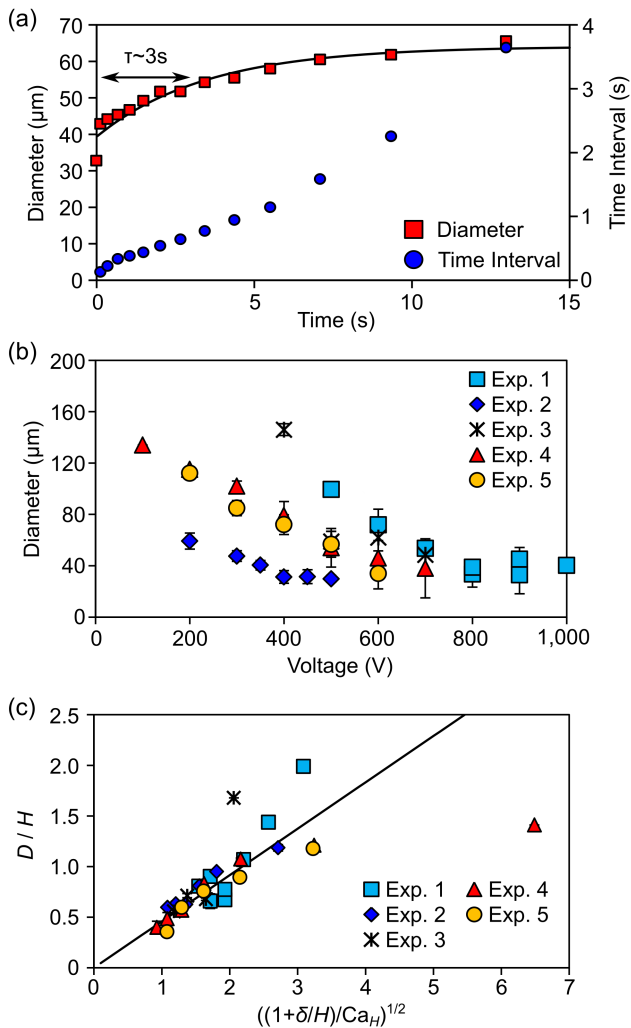
FIG. 2. (a) Drop diameter (red squares) and time interval between successive drops (blue circles) as a function of time for a single experiment under ideal conditions (Experiment 6, $V = 400$ V, $p'_w = 0.12$ psi). The black curve is an exponential fit with a characteristic time scale of 3 s. (b) Average drop diameter vs applied voltage for experiments $1 - 5$ (see Table I). In each experiment, the inlet water pressure was set just below that required to flood the central channel. (c) Data from (b) collapse onto a single line when scaled according to Eq. (1). The black line is a linear fit to the data for small drops ($D < H$) with slope 0.46 and $R^2 = 0.98$.

1. Drop Size

The size of the water drops decreased with increasing applied voltage (Fig. 2b). As summarized in Table I, we varied several key parameters to determine their respective impacts on the size of the resulting drops. The addition of surfactant decreased the oil-water tension and resulted in smaller drop diameters (cf. experiments 1 and 2 in Fig. 2b). Decreasing the scale of the microfluidic channels caused the drop size to decrease (cf. experiments 2 and 3). Increasing the viscosity of the water phase by a factor of two by addition of glycerol (30 wt%) had little impact on the drop size (cf. experiments 4 and 5).

These qualitative trends can be understood through a scaling analysis that balances the electric force on the charged droplet with that due to capillarity [35]. The applied field $E \sim V/W$ induces a capacitive charge on a conductive drop of order $q \sim \varepsilon D^2 E$ [36]. The action of the field on the charged drop leads to an electric force $F_e \sim qE \sim \varepsilon D^2 E^2$, which competes with the capillary force that holds the drop to the rectangular nozzle $F_c \sim \gamma(H + \delta)$. As the drop grows, the electric force increases and ultimately exceeds that due to capillarity causing the drop to detach from the nozzle. This picture leads to the following expression for the drop size at pinch-off

$$D \sim H\sqrt{\frac{(1 + \delta/H)}{\mathrm{Ca}_H}}, \qquad (1)$$

where $\mathrm{Ca}_H = \varepsilon E^2 H/\gamma$ is an electric Capillary number, and the ratio of the nozzle size to the channel height is typically small, $\delta/H \ll 1$. Using this relation, the data in Figure 2b collected at various conditions can be collapsed onto a single line when the drop size is smaller than the channel height (Fig. 2c). The behavior of larger, disk-like drops is not captured by the above relation. Further deviations from the proposed scaling law may be caused by electrostatic and/or hydrodynamic interactions between successive drops (see below). Physically, the system is like a dripping faucet that uses electrostatic rather than gravitational force to drive drop formation.

2. Drop Frequency

The frequency at which drops were generated increased with the magnitude of the applied voltage (Fig. 3a). Below some critical voltage, no drops were generated. We further observed that a two fold increase in the viscosity of the aqueous phase caused the drop frequency to decrease by a similar factor. To understand these trends, it is helpful to examine size of a single drop as a function of time (Fig. 3b). Following pinch-off, the water-oil interface moves slowly through the narrow nozzle. Once the drop begins to grow, it does so rapidly at a nearly constant volumetric rate. The frequency of drop generation is therefore determined by the slower process of interface motion through the nozzle.

The observed characteristics of the drop filling process are well captured by a scaling analysis that accounts for the electric and capillary stresses at the oil-water interface (Fig. 3c). Within the nozzle, the capillary pressure across the interface can be approximated as $2\gamma/\delta(x)$, where $\delta(x)$ is the local width of the nozzle. For simplicity, we assume that the channel width is smallest at $x = 0$ and grows slightly in either direction (Fig. 3c). The electric stress normal to the interface is $\frac{1}{2}\varepsilon E^2$, where E is the magnitude of the local field at the surface of the conductive drop. The total pressure

drop across the water channel can then be approximated as $\Delta p(x) = p'_w - 2\gamma/\delta(x) + \frac{1}{2}\varepsilon E^2$, where p'_w is the inlet water pressure less the gravitational pressure difference between the pump and the device.

Prior to application of the field ($E = 0$), the pressure drop is zero, and the interface sits at a stable position upstream of the most narrow point ($x < 0$). The electric stress induced by the applied voltage results in a finite pressure drop, which drives flow through the water channel at a volumetric rate $Q = \Delta p/R_w$, where R_w is the hydrodynamic resistance of the water channel (Appendix A). This linear relation between the flow rate and the pressure drop is appropriate for the laminar flows described here (the Reynolds number during drop filling was at most Re $= \rho Q/H\eta \sim 40$). As in experiment, a finite voltage is required to drive flow through the most narrow region of the nozzle (i.e., $\Delta p(0) > 0$). Above this critical voltage, the characteristic pressure drop remains quite small ($\Delta p(0) \ll p'_w$), and flow through the nozzle is slow (Fig. 3b). Upon exiting the nozzle, the drop curvature decreases, and the dominant contribution to the pressure drop is the applied pressure p'_w, which is ca. 10^2 times larger than the electric stress. The drop then grows rapidly until it detaches from the nozzle. The rate of drop growth inferred from Figure 3b ($Q = 3.7$ nL/s) is in qualitative agreement with that predicted based on the estimated resistance of the water channel (i.e., $Q = p'_w/R_w = 2.5$ nL/s). Under these conditions, the rate limiting process for drop generation is the slow motion of the interface through the nozzle.

Based on the above analysis, the voltage-dependence of the drop frequency should have the approximate form $f = A[(V/V^*)^2 - 1]$. Here, the threshold voltage V^* depends on the nozzle geometry and the applied pressure but not on the viscosity of the fluid. By contrast, the constant A is inversely proportional to the hydrodynamic resistance and therefore the fluid viscosity. These predictions are consistent with the experimental results shown in Figure 3a. Liquids of different viscosities showed the same critical voltage $V^* = 315$ V; the ratio of the fitted A constants was nearly identical to that of the water viscosities ($A_5/A_4 = 1.9$ vs $\eta_4/\eta_5 = 2$ where the subscript denotes the experiment number).

3. Electrohydrodynamic Instabilities

For sufficiently large voltages, the dripping regime described above became unstable. Under these conditions, the initially curved oil-water interface developed a sharp Taylor cone [16, 37] that ejected small daughter droplets into the central channel in an erratic fashion. Physically, such electrohydrodynamic instabilities arise when the normal electric stress at the interface exceeds the capillary pressure. Electrospraying occurred most readily when the interface was confined within the narrow nozzle region. At intermediate voltages, electrospray events did not prohibit the formation of larger drops; however, they
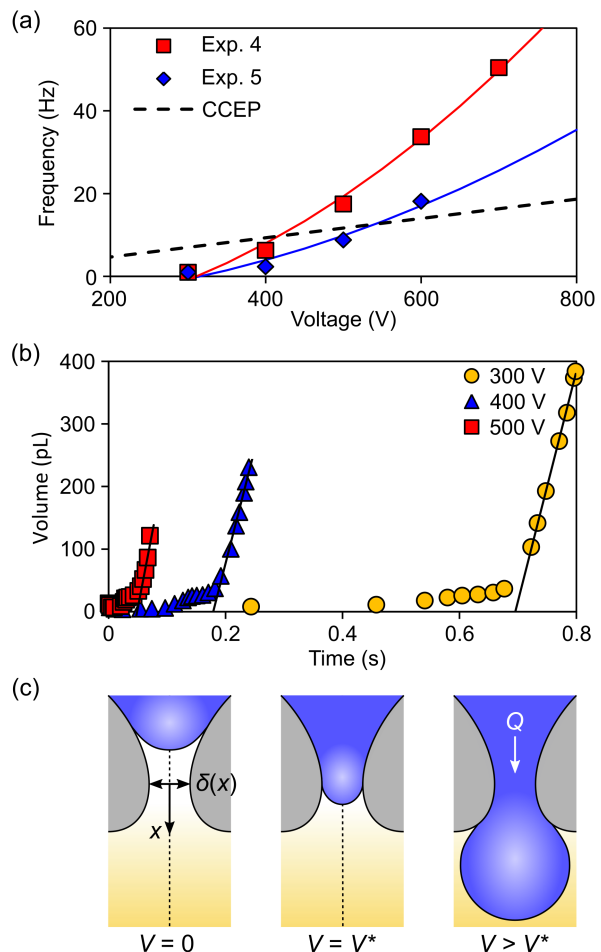

FIG. 3. (a) Average drop generation frequency f vs voltage V for two different water viscosities. Data are from experiments 4 and 5 in Table I. The solid curves show fits of the form $f = A[(V/V^*)^2 - 1]$. The dashed curve shows the predicted frequency for CCEP oscillations $f = U_0/W$. (b) Drop volume vs time during the generation of the second drop. For each voltage, the time range starts at pinch-off of the first drop and continues until pinch-off of the second drop. Data are from experiment 5. The solid lines are linear fits showing a constant volumetric flow rate of $Q = 3.7$ nL/s. (c) Schematic illustration of the different stages of drop generation.

did increase the variability in the drop size. Additionally, the presence of small water droplets in the channel was observed to interfere with the charging and actuation of larger drops down the ratcheted channel. It was therefore desirable to operate at sufficiently low voltages as to avoid the onset of electrospraying. The threshold voltage above which electrospraying occurred depended on the detailed geometry of the microfluidic system; for the conditions of experiments $3-5$ (Table I), this voltage was between 400 and 500 V.

B. Drop Transport

Once generated, the charged drops were transported down the ratcheted channel in a manner similar to that of solid conductive spheres reported previously [20]. Unlike solid particles, however, aqueous drops can deform in response to electric stresses acting at their interface. Drop deformation is opposed by surface tension, which favors spherical drops that minimize the interfacial area. The relative importance of these competing forces is characterized by the electric capillary number $Ca_D = \varepsilon E^2 D/\gamma$. For small capillary numbers $Ca_D \ll 1$, the drop is expected to behave like a non-deformable sphere. For sufficiently large capillary numbers ($Ca_D > 0.42$), a conductive drop becomes unstable in a uniform electric field resulting in the ejection of charged droplets from Taylor cones at the poles [38, 39]. We observed that drops were stable in the applied field for capillary numbers $Ca_D < 0.7$, which is somewhat larger than the previously reported threshold. This discrepancy is attributed to the fact that the electric field strength in the center of the channel is somewhat less than the approximate value V/W used to compute Ca_D (Fig. S3) [22, 29]. We performed experiments at intermediate capillary numbers ($0.04 < Ca_D < 0.7$) and measured the velocity U of drops positioned in the center of the channel moving in the direction parallel to the electric field. Measured velocities ranged from $1 - 10$ mm/s; the mean velocity of the drop down the length of the channel was typically an order of magnitude smaller (Fig. S4) [29].

To compare drop motions under different experimental conditions, we scaled the measured velocity by that predicted for a spherical drop under idealized conditions [40]. On contact with a planar electrode, a conductive sphere should acquire a net charge $q = \frac{1}{6}\pi^3 \varepsilon D^2 E$ such that its electric potential is equal to that of the electrode [36]. Neglecting interactions between the charged sphere and its image, the resulting electric force is well approximated as $F_e = qE$ [36]. This electric force is balanced by the hydrodynamic drag on the spherical drop as it moves through its viscous surroundings. For a spherical drop moving through an unbounded fluid of high viscosity ($\eta_0 \gg \eta_w$), the drag force can be approximated as $F_h = 2\pi\eta_o D U_0$ [41]. Balancing $F_e = F_h$, the predicted velocity of the drop is $U_0 = \pi^2 \varepsilon D E^2/12\eta_o$.

Figure 4a plots the measured drop velocity scaled by the predicted value U/U_0 as a function of the drop diameter scaled by the channel height D/H for experiments $1-5$ summarized in Table I. Drops of different sizes were created by varying the applied voltage V and/or the inlet water pressure p_w (Fig. S5) [29]. For experiments $2-5$ with lower interfacial tension, the data collapse onto a single curve, in which the scaled velocity decreases with increasing drop size. These experiments differ in the size of the channel, the viscosity of the liquids, and the voltages applied. Their collapse onto a single curve implies that the predicted dependence on the electric field and the oil viscosity are correct. Moreover, the measured

velocity approaches the predicted value when the size of the drop is much less than the height of the channel (i.e., as $D/H \to 0$). These observations suggest that the systematic discrepancy between measured and predicted velocities is due to the hydrodynamic resistance imposed by the channel walls on drop motion. This hypothesis is further supported by finite element calculations of the hydrodynamic resistance for a spherical drop moving near the wall of a cubic channel of size H (Appendix B). Accounting for the additional resistance, the predicted drop velocity is in qualitative agreement with the experimental observations (dashed curve in Fig. 4a).
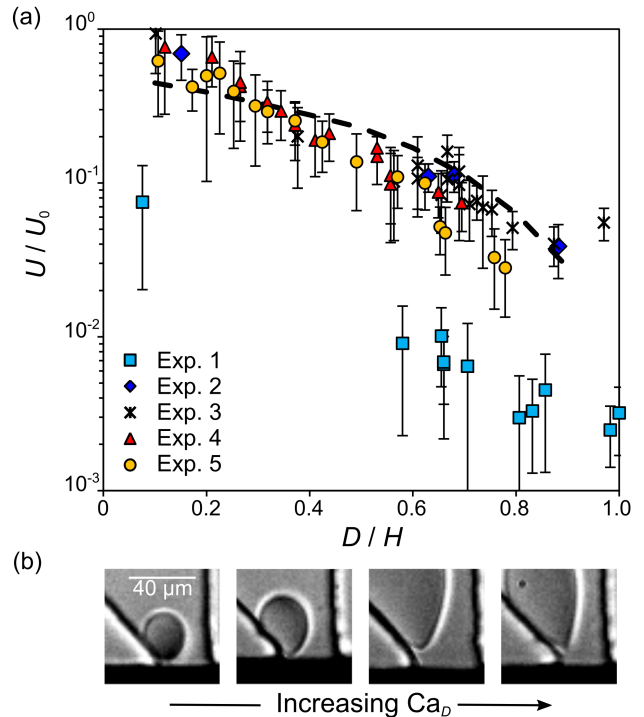

FIG. 4. (a) Drop velocity U scaled by the predicted value U_0 as a function of drop size D scaled by the channel height H for the experimental systems summarized in Table I. Colored markers denote the mean of ca. 10 measurements made on each drop; error bars represent one standard deviation above and below the mean. The dashed curve represent the predicted drop velocity when accounting for the increased hydrodynamic resistance due to the channel walls (see Supplemental Material). (b) Characteristic images of charged droplets approaching an oppositely biased electrode immediately prior to reversing direction. The capillary number $Ca_D = \varepsilon D E^2/\eta$ increase from left to right as 0.11, 0.13, 0.29, and 0.48.

In experiment 1 with no added surfactant, the dependence of the drop velocity on drop size was similar to that of the other experiments; however, the magnitude of the velocity was roughly an order of magnitude smaller (Fig. 4a). One possible explanation for this observation is that these drops acquired less charge on contact with the gallium electrodes. The range of capillary numbers explored in experiment 1 was similar to that of the other

experiments ($0.04 < \mathrm{Ca}_D < 0.4$). As a result, the drops experienced similar field-induced deformations prior to contact with either electrode (Fig. 4b). However, owing to their larger interfacial tension, drops in experiment 1 were subject to stronger electric fields than those in other experiments. Applied electric fields were as large as 4 V/μm, which is close to the dielectric strength of mineral oil. Under these conditions, drops may acquire charge through an electric discharge prior to physical contact of the interface with the electrode; this mechanism is believed to be responsible for the charging of solid conductive particles under similar conditions [22]. By contrast, drops with lower surface tension at weaker fields (experiments $2-5$) may charge through a transient liquid bridge, which forms between the drop and the electrode. Such qualitative differences in the mechanisms of contact charging may help to explain the significant differences observed for drops of different surface tensions. Further study is required to more fully understand the physics of drop charging on contact with biased electrodes.

C. Optimal Operating Conditions

Having identified the basic physical mechanisms underlying electric drop generation and ratcheted transport, we now consider the integration of these two components within a single device powered by a common voltage input. There are three key conditions that must be satisfied for the reliable generation and transport of drops. First, the applied voltage must be sufficiently small as to avoid electrohydrodynamic instabilities, which can lead to heterogeneous drop sizes or even a short-circuit. Second, the drop diameter must be sufficiently small relative to the features of the ratcheted channel to allow steady transport. Finally, the drop generation frequency must be sufficiently small relative to that of CCEP oscillations, such that drops – once generated – are quickly transported away from the nozzle. In experiment, these conditions can be satisfied by appropriate tuning of the applied voltage V and the inlet water pressure p_w as illustrated by the "phase diagram" of Figure 5a. Below we discuss the different ways that the system malfunctioned when these conditions were not satisfied.

When drops were generated too rapidly from the nozzle, the later drops were observed to interfere with the ratcheted transport of earlier drops. Under these conditions, drops often organized to form a dynamic oscillating chain similar to those reported by Ristenpart and co-workers [33] (Fig. 5, blue). Within this chain, multiple drops moved in the field and exchanged charge on contact. Ultimately, the chain would span the channel between the nozzle and the lower electrode, thereby preventing further drop generation and transport. We refer to this behavior as "jamming" (Fig. 5, blue), which can be avoided by reducing the frequency at which drops are generated. As discussed above, the drop frequency is controlled by the movement of the oil-water interface
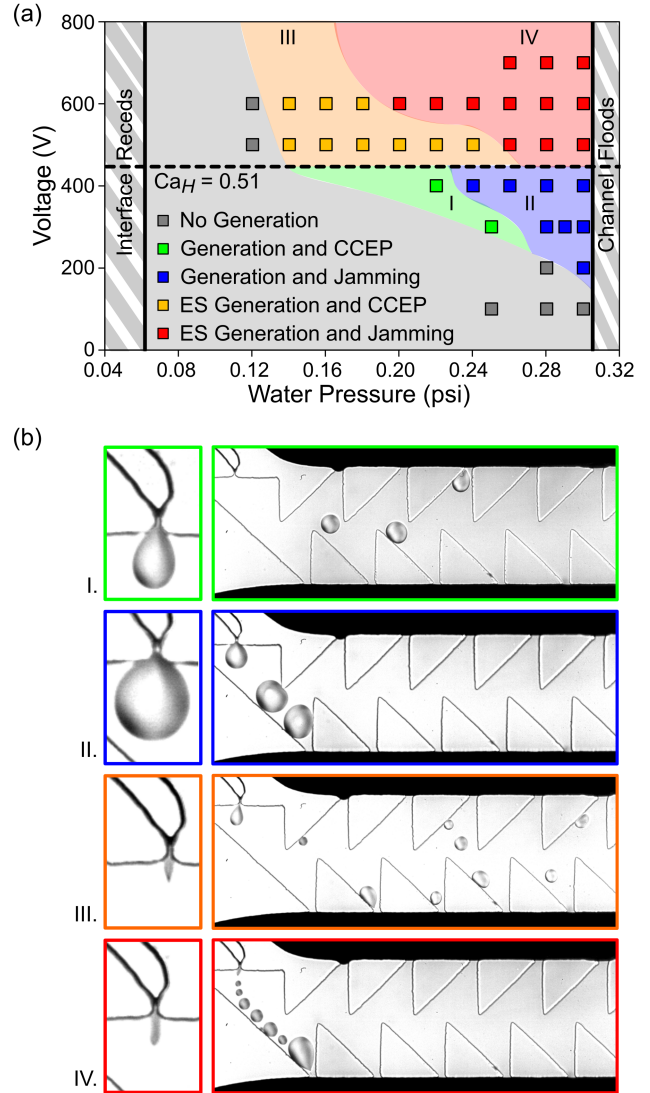

FIG. 5. (a) Phase diagram of drop generation and transport as a function of applied voltage V and water pressure p'_w for experiment 4. Markers representing individual experiments are colored based on the qualitative behaviors listed in the legend. The colored regions are only to guide the eye. The upper and lower pressure limits correspond to the flooding and receding pressures, respectively. (b) Representative images of droplet generation (left) and transport behavior (right) illustrating the qualitative behaviors in (a). Representative videos for regions I-IV are provided in the Supplemental Materials [29].

through the nozzle, which can be slowed by reducing the inlet water pressure and/or the hydrodynamic resistance of the water channel. Note, however, that this pressure must remain sufficiently large as to move the interface through the narrow nozzle with the help of the electric stress. The optimal operating pressure lies between these two limits (Fig. 5, green).

When the applied voltage was larger than 400 V (for experiment 4), electrohydrodynamic instabilities were

observed at the water nozzle (Fig. 5, orange and red). Under these conditions, the drop interface at the nozzle became sharply pointed and moved erratically due to ejection of small charged droplets (often too small to be observed by our microscope). Such instabilities did not prevent formation of larger drops; however, their sizes were significantly more polydisperse than those created in the absence of electrohydrodyanmic instabilities. Owing to the larger electric fields and accompanying stresses, drop generation could be achieved at lower water pressures (Fig. 5, orange). At low voltages, the system could fail in several different ways depending on the specific conditions (Fig. 5, gray). For smaller nozzles, the applied voltage was often unable to move the interface to initiate the first drop. For large nozzles, the first drop would initiate but never detach from the nozzle thereby flooding the central channel with water. Even when drops did form, their large size could prohibit their movement through the ratcheted channels.

The generation of polydisperse droplet sizes at higher voltages caused successive drops to move at different speeds down the ratcheted channel; here, smaller drops moved faster than larger ones. Owing to the non-coalescence of oppositely charged drops in an electric field, [33, 34] faster moving drops were frequently observed to "pass" slower traffic ahead in a manner similar to that observed for solid particles [20]. This behavior was only observed for conductive drops (with 100 mM NaCl), which exchange charged rapidly and move apart prior to coalescence. By contrast, weakly conductive drops (without added NaCl) were frequently observed to coalesce on contact as reported previously [34]. Moreover, we observed that even conductive drops (with 100 mM NaCl) can coalescence when they approach one another along a vector perpendicular to the applied field.

Overall, the parameter space corresponding to reliable generation and transport of drops is rather small; however, it can likely be enlarged by further modifications to the current design. In particular, there does not appear to be a significant advantage to having a small nozzle (i.e., $\delta \ll H$); increasing the size of this nozzle may help to increase the threshold voltage for electrohydrodynamic instabilities and lower the flooding pressure (and thereby the drop frequency). Additionally, the drop frequency can be reduced to avoid jamming by increasing the hydrodynamic resistance of the water channel (as opposed to decreasing the inlet pressure). While our present experiments relied on external pumps for convenience, the small pressure drops required for optimal operation are readily achieved using gravity and can perhaps be eliminated by controlling the wettability of the water channel. The pressure head for the current designs is ca. 15 cm and can be further reduced to ca. 3 cm by increasing the size of the nozzle such that $\delta \sim H$.

These considerations are relevant to achieving portable microfluidic systems based on the active generation and manipulation of droplets. In this context, it is important to recognize that the contents of the conductive drop are effectively screened from the electric field and that the amount of charge transferred on contact is negligible compared to the number of charge carriers within the drop (typically, 1 in 10^6). Consequently, CCEP can be used to manipulate drops containing reactive biochemical species[24, 26] and even mammalian cells[42, 43] without interfering with reaction progress or cell viability. Additionally, the relatively high voltages required by CCEP are readily supplied by miniature, battery-powered amplifiers [44]. These ~1 cm^3-scale components are commercially available and have been used in portable microfluidic applications such as analytical separations based on capillary electrophoresis [45].

IV. CONCLUSIONS

We demonstrated that aqueous drops can be steadily generated and transported within microfluidic systems using a single input voltage and very low power (ca. 10 nW). Our analysis of the basic physics governing droplet size, generation frequency, and transport velocity should prove useful in the rational design of future systems for manipulating drops using contact charge electrophoresis. We argue that such systems could offer key advantages in terms of simplicity and portability as compared to existing platforms for droplet-based microfluidics. In particular, the ability to transport droplets via ratcheted CCEP eliminates the need for external pumps and/or arrays of independently controlled electrodes require by alternative methods. However, several challenges remain to be addressed before these advantages can be fully realized. The present system allowed for sustained operation for only few seconds before the electric field was significantly altered by the accumulation of charge at the PDMS-oil interface. In principle, such charge accumulation can be avoided by matching the electrical conductivity of the PDMS ramps to that of the oil; we are currently working to implement this strategy to enable the continuous electric generation of monodisperse drops. Further study is also required to understand the details of droplet charging on contact with solid electrodes. For example, the ability to control the presence and/or amount of water deposited onto the electrodes during contact charging could be important for preventing cross-contamination between otherwise independent drop-based reactors. Despite these challenges, we believe that electrostatic transport mechanisms like CCEP can contribute to microfluidic-based applications ranging from "on-site" drug formulation to droplet digital PCR.

Appendix A: Hydrodynamic Resistance of the Water Channel

For fully developed laminar flow, the flow rate through a microfluidic channel is linearly related to the pressure drop as $Q = \Delta p / R$, where R is hydrodynamic resistance. The hydrodynamic resistance of a rectangular channel can be expressed as [46]:

$$R = \frac{12\eta L}{H^3 W}\left(1 - \sum_{n=1}^{\infty} \frac{192 H \tanh[(2n-1)\pi H/2W]}{(2n-1)^5 \pi^5 W}\right)^{-1},$$
(A1)

where η is the fluid viscosity, and H, W, and L are the height, width, and length of the channel, respectively (assuming $H < W$). For channels with multiple segments of different geometries in series, the resistances can be summed to find the equivalent resistance for the entire device. For the experiments 4 and 5, a long winding channel was designed upstream of the water inlet (with $H = 50$ μm, $W = 95$ μm, and $L = 0.23$ m), resulting in a hydrodynamic resistance of $R_w = (3 \times 10^{17}\ \mathrm{m}^{-1})\eta_w$ as quoted in the main text. In these experiments, the resistance of the water channel was much larger than all other components of the microfluidic system.

Appendix B: Hydrodynamic Drag on a Drop in Channel

We used a finite element solver (COMSOL) to compute the hydrodynamic resistance of a spherical drop of diameter D moving within a cubic channel of dimension H (Fig. 6). The surface of the drop is assumed to contact the center of the channel wall at $z = 0$; in experiment, the denser water drops are expected to sediment to the floor of the channel. The drop moves in the y-direction with a constant velocity $\boldsymbol{U} = U\boldsymbol{e}_y$. At low Reynolds numbers, the pressure p and velocity $\boldsymbol{u}$ surrounding the drop are governed by the Stokes equations

$$0 = \nabla \cdot \boldsymbol{\sigma} = -\nabla p + \eta \nabla^2 \boldsymbol{u},$$
(B1)

$$0 = \nabla \cdot \boldsymbol{u},$$
(B2)

where $\boldsymbol{\sigma}$ is the stress tensor, and η is the viscosity of the carrier fluid. We assume no-slip boundaries at the walls of the channel

$$\boldsymbol{u} = 0 \text{ for } \boldsymbol{x} \in \text{channel wall}.$$
(B3)

At the surface of the drop, there is no flow normal to the interface except that due to motion of the drop as a whole

$$\boldsymbol{u} \cdot \boldsymbol{n} = \boldsymbol{U} \cdot \boldsymbol{n} \text{ for } \boldsymbol{x} \in \text{drop surface},$$
(B4)

where $\boldsymbol{n}$ is the outward facing unit vector normal to the drop surface. As the viscosity of the fluid inside the drop is much less than that of the surrounding fluid, we assume there are no tangential stresses at the drop surface

$$\boldsymbol{t} \cdot \boldsymbol{\sigma} \cdot \boldsymbol{n} = 0 \text{ for } \boldsymbol{x} \in \text{drop surface},$$
(B5)

where $\boldsymbol{t}$ is a unit vector tangent to the drop surface. Solving the above equations numerically, the drag force is obtained by integrating the stress over the surface of the drop

$$\boldsymbol{F} = \int_S \boldsymbol{n} \cdot \boldsymbol{\sigma}\, dS = \lambda \boldsymbol{U}.$$
(B6)

This force is linearly proportional to the drop velocity with a calculated resistance greater than that expected for a drop in an unbounded fluid, $\lambda > 2\pi\eta D$.
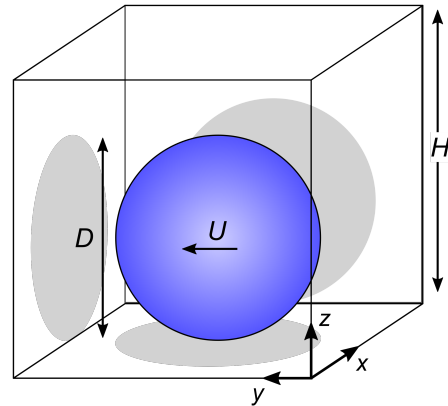

FIG. 6. Schematic illustration of the model geometry for a spherical drop moving in a cubic channel.

[1] H. Song, D. L. Chen, and R. F. Ismagilov, Angew. Chem. Int. Ed. **45**, 7336 (2006).
[2] A. Huebner, S. Sharma, M. Srisa-Art, F. Hollfelder, J. B. Edel, and A. J. DeMello, Lab Chip **8**, 1244 (2008).
[3] S.-Y. Teh, R. Lin, L.-H. Hung, and A. P. Lee, Lab Chip **8**, 198 (2008).
[4] M. T. Guo, A. Rotem, J. A. Heyman, and D. A. Weitz, Lab Chip **12**, 2146 (2012).
[5] M. Abolhasani and K. F. Jensen, Lab Chip **16**, 2775 (2016).
[6] K. Churski, P. Korczyk, and P. Garstecki, Lab Chip **10**, 816 (2010).
[7] C. A. Stan, G. F. Schneider, S. S. Shevkoplyas, M. Hashimoto, M. Ibanescu, B. J. Wiley, and G. M. Whitesides, Lab Chip **9**, 2293 (2009).
[8] C. A. Stan, S. K. Y. Tang, K. J. M. Bishop, and G. M. Whitesides, J. Phys. Chem. B **115**, 1089 (2011).
[9] L. Mazutis, J. Gilbert, W. L. Ung, D. A. Weitz, A. D. Griffiths, and J. A. Heyman, Nat. Protoc. **8**, 870 (2013).
[10] S. L. Anna, Annu. Rev. Fluid Mech. **48**, 285 (2016).

[11] A. Sciambi and A. R. Abate, Lab Chip **15**, 47 (2015).

[12] K. Choi, A. H. Ng, R. Fobel, and A. R. Wheeler, Annu. Rev. Anal. Chem. **5**, 413 (2012).

[13] D. G. Rackus, M. H. Shamsi, and A. R. Wheeler, Chem. Soc. Rev. **44**, 5320 (2015).

[14] A. W. Martinez, S. T. Phillips, G. M. Whitesides, and E. Carrilho, Anal. Chem. **82**, 3 (2010).

[15] A. K. Yetisen, M. S. Akram, and C. R. Lowe, Lab Chip **13**, 2210 (2013).

[16] G. I. Taylor, Proc. R. Soc. A **280**, 383 (1964).

[17] R. T. Collins, J. J. Jones, M. T. Harris, and O. A. Basaran, Nat. Phys. **4**, 149 (2008).

[18] D. R. Link, E. Grasland-Mongrain, A. Duri, F. Sarrazin, Z. Cheng, G. Cristobal, M. Marquez, and D. A. Weitz, Angew. Chem. Int. Ed. **45**, 2556 (2006).

[19] Z. Z. Chong, S. H. Tan, A. M. Ganan-Calvo, S. B. Tor, N. H. Loh, and N.-T. Nguyen, Lab Chip **16**, 35 (2016).

[20] A. M. Drews, H.-Y. Lee, and K. J. M. Bishop, Lab Chip **13**, 4295 (2013).

[21] M. Kowalik and K. J. M. Bishop, Appl. Phys. Lett. **108**, 203103 (2016).

[22] A. M. Drews, C. A. Cartier, and K. J. M. Bishop, Langmuir , 3808 (2015).

[23] Y. Dou, C. Cartier, W. Fei, S. Pandey, S. Razavi, I. Kretzschmar, and K. Bishop, Langmuir **32**, 13167 (2016).

[24] D. J. Im, J. Noh, D. Moon, and I. S. Kang, Anal. Chem. **83**, 5168 (2011).

[25] D. J. Im, M. M. Ahn, B. S. Yoo, D. Moon, D. W. Lee, and I. S. Kang, Langmuir **28**, 11656 (2012).

[26] D. J. Im, B. S. Yoo, M. M. Ahn, D. Moon, and I. S. Kang, Anal. Chem. **85**, 4038 (2013).

[27] Y. Xia and G. M. Whitesides, Annu. Rev. Mater. Sci. **28**, 153 (1998).

[28] J.-H. So and M. D. Dickey, Lab Chip **11**, 905 (2011).

[29] See Supplemental Material at [URL will be inserted by publisher] for additional figures showing I. Gallium electrodes, II. Tensiometry Measurements, III. Electric field in the channel, IV. Droplet velocity down the channel, and V. Effect of water pressure on drop diameter.

[30] C. A. Cartier, A. M. Drews, and K. J. M. Bishop, Lab Chip **14**, 4230 (2014).

[31] R. Dangla, F. Gallaire, and C. N. Baroud, Lab Chip **10**, 2972 (2010).

[32] I. D. Morrison, Colloids Surfaces A Physicochem. Eng. Asp. **71**, 1 (1993).

[33] W. D. Ristenpart, J. C. Bird, A. Belmonte, F. Dollar, and H. A. Stone, Nature **461**, 377 (2009).

[34] B. S. Hamlin, J. C. Creasey, and W. D. Ristenpart, Phys. Rev. Lett. **109**, 094501 (2012).

[35] N. Vilanova, V. R. Gundabala, and A. Fernandez-Nieves, Applied Physics Letters **99**, 2 (2011).

[36] A. M. Drews, M. Kowalik, and K. J. M. Bishop, J. Appl. Phys. **116**, 074903 (2014).

[37] J. Fernández de la Mora, Annu. Rev. Fluid Mech. **39**, 217 (2007).

[38] C. G. Garton and Z. Krasucki, Proc. R. Soc. A Math. Phys. Eng. Sci. **280**, 211 (1964).

[39] J. D. Sherwood, J. Fluid Mech. **188**, 133 (1988).

[40] J. S. Eow and M. Ghadiri, Chem. Eng. Process. **42**, 259 (2003).

[41] J. F. Harper, Adv. Appl. Mech. **12**, 59 (1972).

[42] D. J. Im, J. Noh, N. W. Yi, J. Park, and I. S. Kang, Biomicrofluidics **5**, 44112 (2011).

[43] C. P. Lee, H. C. Chang, and Z. H. Wei, Appl. Phys. Lett. **101**, 014103 (2012).

[44] D. Erickson, D. Sinton, and D. Li, Lab Chip **4**, 87 (2004).

[45] C. D. García, Y. Liu, P. Anderson, and C. S. Henry, Lab Chip **3**, 324 (2003).

[46] N.-T. Nguyen, *Micromixers Fundamentals, Design and Fabrication*, 2nd ed. (Elsevier Inc., 2012) pp. 14–19.